Journal Title
XX(X):1–16

DOI: 10.1177/ToBeAssigned
www.sagepub.com/
SAGE

# Diffusion performance of lobed jet in the developed states consistent across temporally and spatially developing flows

**Mamoru Takahashi[1], Ren Fukui[2], Koichi Tsujimoto[1] and Toshitake Ando[1]**

**Abstract**

This study demonstrates that temporally developing lobed jets can qualitatively reproduce the diffusion performance in the fully developed states of spatially developing lobed jets in laboratory experiments. The jet exit geometries, Reynolds number ($= 70,000$), and turbulence intensity (3% of mean velocity) were set to be the same across the temporally and spatially developing jets. Four types of jet flows were tested, one being a round jet and three being lobed jets with different numbers or curvatures of lobes, referred to as 6L, 6S, and 3L, respectively. The half-width of the mean streamwise velocity distributions and centerline mean streamwise velocity of the four jets in the developed states were consistent between the numerical simulations and experiments. The round jet displayed the highest diffusion performance, followed by 3L, while 6L and 6S were the smallest and were comparable with each other. Despite such consistency in the developed states, the diffusion performance and formation of the streamwise swirling flows did not agree between the numerical and experimental results. These results suggest that unique large-scale structures corresponding to the initial conditions are reproduced in temporally developing jets, which is in good agreement with the spatially developing lobed jets. Therefore, the current study demonstrated that the temporally developing simulations can reproduce similar diffusion processes to those of the spatially developing ones.

**Keywords**

Jet, Turbulent Mixing, Hot-Wire Anemometry, Large-Eddy Simulation

## Introduction

Fluid mixing by turbulent jets occurs in countless industrial situations, such as chemical plants, combustion, or air conditioners. Accurate prediction of the diffusion performance of turbulent jets is important for improving the efficiency of such mixing equipment, thereby saving energy. However, for many years, the prediction of jet diffusion performance has relied strongly on empirical rules. Because this requires inefficient trial-and-error in equipment design, it is strongly desirable to combine jet equipment design and diffusion performance.

Early understanding of jets assumed that they lost memories of upstream (initial) conditions during their development and that statistical properties are universal regardless of the upstream conditions in the developed state. However, as reviewed in George[1], a large body of experimental evidence has reported asymptotic effects of the initial and upstream conditions. Specifically, even if universal features are observed in the non-dimensional functions of the vertical distribution of first- or second-order moments, local characteristic scales (mean streamwise velocity along the centerline and half-width of the vertical mean velocity distribution) show unique results depending on the upstream conditions[2–4]. This suggests that the diffusion performance of the jet can be easily modified or controlled by upstream conditions. Based on this idea, many studies have attempted to determine the optimum jet flow conditions for obtaining the desired diffusion effect. The velocity distribution at the exit was modified by changing the contraction of the flow in the nozzle, such as smooth contraction, orifice, and pipe[5–10]. Jets issued from nozzles with non-circular geometries, such as elliptical, triangular, and rectangular, were also tested, and some of them showed a higher mixing effect than those with circular geometries[11–17].

It is believed that the diffusion performance of developed shear flows is determined by certain large-scale structures. For example, in plane jets, antisymmetric arrangements of large-scale vortices have been observed[18–23]. Meanwhile, large-scale helical structures have been detected in round jets: not only single-helices but also double- or even triple-helices have been observed in other studies[24–31]. It has been confirmed that these structures carry large amounts of turbulence energy and contribute to the turbulent momentum exchange. Therefore, we consider that the jets may form unique large-scale dominant structures in developed states according to their exit geometries.

To detect the spatial structures, numerical simulation of the jet is useful because it outputs full spatiotemporal flow

[1]Mie University, JP
[2]The Japan Steel Works, Ltd, JP

**Corresponding author:**
Mamoru Takahashi, Mie University, Kurimamachiya-cho 1577, Tsu, Mie, JP.
Email: takahashi@mach.mie-u.ac.jp

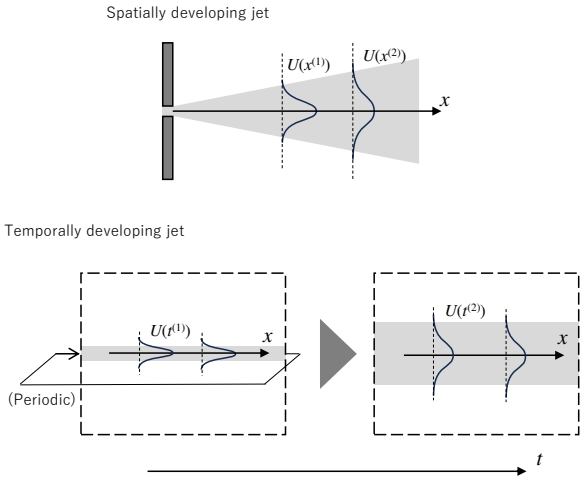


**Figure 1.** Schematic of spatially and temporally developing jets.

datasets. While the numerical flows simulating the flow fields in the laboratory experiments are referred to as "spatially developing flows", one can also simulate "temporally developing flows" instead. This can be accomplished by imposing periodic boundary conditions in the streamwise direction. When an initial columnar high-speed jet core is released in the numerical domain, it diffuses and decays with time, resulting in (statistically) an unsteady but streamwise homogeneous jet field. A graphical explanation was provided in Fig. 1. The principal advantage of temporally developing simulations is homogeneity, which is more beneficial for the investigation of turbulent structures than using spatially developing ones. The temporally developing simulations were widely used to study a variety of shear flows, not only the jets[32–41], but also mixing layers[42], wakes[43], and boundary layers[44,45].

In the authors' recent study, a simulation of a temporally developing round jet was employed to investigate the large-scale dominant structures in the round jet in the developed state[31]. Owing to the spatial periodicity, the results from a spatial oscillation analysis based on Koopman decomposition clearly illustrated the spatiotemporal behavior of the dominant structures. We hope that simulations of temporally developing jets may reveal the modification of the dominant structures in the far fields from the exits according to the jets' initial conditions and their influence on the jet diffusion performance. However, it is crucial to compare the characteristics of temporally developing jets with spatially developing ones because temporally developing jets are idealized and can never be formed in any fluid flow device in the laboratory. If the statistical properties are consistent with each other, even qualitatively, we will have a reasonable justification to consider that the dominant structures in the temporally developing jets are also essential in laboratory experiments. This study was conducted to demonstrate that temporally developing flow simulations can reproduce the diffusion performance, which is consistent with the results of laboratory experiments.

In this study, we tested several non-circular exit geometries; however, we note that there were infinite combinations of the tested non-circular geometries. We considered employing lobed geometries that are characterized by their wavy edges and can be determined by varying the number of lobes and their curvatures[13,46–53]. This non-axisymmetry is intended to generate strong turbulence at the jet ejection and achieve high entrainment of the ambient fluid into the jet core flow. Visualization experiments showed that this turbulence is essentially a longitudinal vortex formed inside and outside the jet. In this study, three-lobed jet geometries, with three or six lobes and large or small curvatures, were tested. In the initial jet states, the Reynolds number and turbulence intensity were identical in the experiments and simulations. Further, the initial mean velocity distributions of all jets were so-called "top hat" due to smooth contraction by the nozzles.

Firstly, we conducted wind tunnel experiments on the round and lobed jets. Through velocity field measurements using hot-wire anemometry, we obtained reference data for the diffusion performance of round and lobed jets. Secondly, we performed large-eddy simulations (LESs) of temporally developing round and lobed jets at the same initial Reynolds number, exit geometries, and turbulence intensity as the experiments. We evaluated our numerical results by qualitative comparison with reference experimental results.

## Experimental details

### *Overview of experimental equipment*

Figure 2 shows a schematic of the experimental equipment. The equipment is roughly split into a jet generator and measurement system. The jet generator consists of an air filter, blower, radiator, and wind tunnel, which are interconnected by piping. The airflow is generated by the blower. The fine dust in the air is removed by the air filter before it is introduced into the piping. The air is somewhat heated due to the compression in the blower but is cooled in the radiator. We carefully monitored the temperature of the ejected air and confirmed that the thermal gap between the ejected air and the surrounding air was within 0.5 °C. The rotation speed of the blower is controlled by a three-phase AC inverter, and the exiting flow speed is determined by turning the frequency of the inverter. The reference flow speed was monitored before and after the main measurement using a digital manometer that was connected to the total pressure tube inserted in the exiting flow.

Figure 3 presents an overview of the wind tunnel. The wind tunnel consisted of two acrylic cylinders: the first cylinder had an inner diameter of 190 mm and length of 245 mm, and the second cylinder had an inner diameter of 70 mm and length of 1020 mm. An acrylic panel (height, 100 mm; width, 100 mm; thickness, 10 mm) was placed at the end of a thinner cylinder on which the round and lobed nozzles were mounted. The airflow introduced into the wind tunnel passes through several devices and channels, as previously described, and is already turbulent. The turbulence of the airflow was removed using two acrylic plates with a through-hole pattern placed in a thicker cylinder. The actual removal of turbulence is confirmed later.

The velocity of the jet air was measured using a hot-wire anemometer (KANOMAX 1010). In this study, we measured one streamwise velocity component (streamwise) using an I-type hot-wire probe (KANOMAX 0251R-T5). The hot-wire system consisted of a tungsten wire with a diameter of 5.0 $\mu$m that was glued together with spot welds in our own

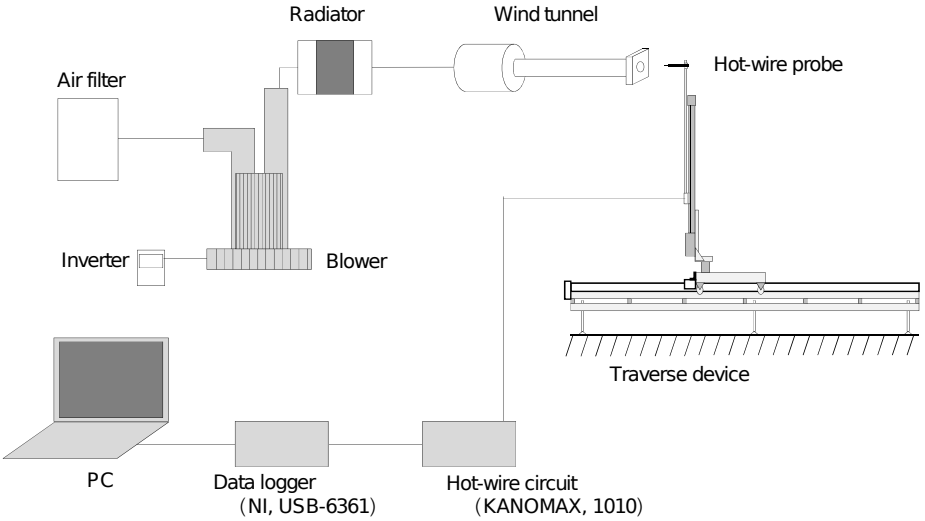


**Figure 2.** Schematic of experimental equipment.

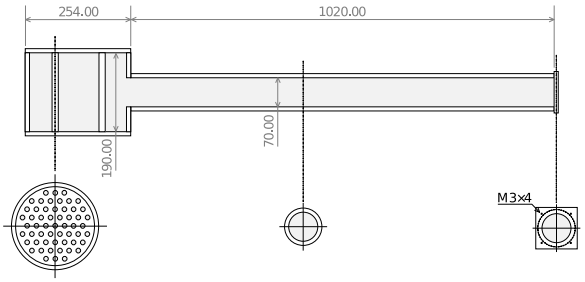


**Figure 3.** Schematic of wind tunnel (unit: mm).

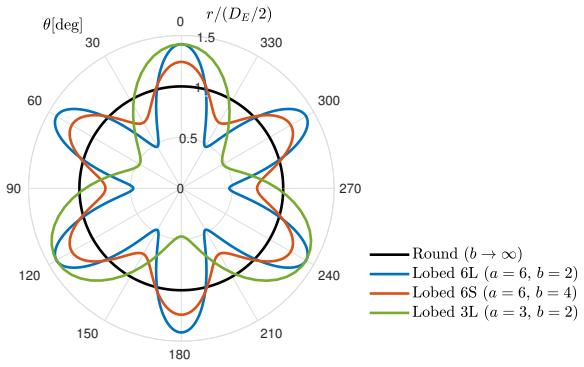


**Figure 4.** Curves produced by Eq. 1 for employed sets of parameters.

work. The hot-wire systems were operated at an overheating ratio of 1.5. The calibration was conducted to obtain the relation between the output voltage and the flow velocity; the hot-wire probe was inserted in the potential core of the jet, and the output voltage varying with the jet velocity was recorded. The voltage-velocity relation was fitted to a fourth-order polynomial using the least-square method.

The hot-wire probe was mounted on a traverse device and stroked in three dimensions. The strokes of the linear actuators corresponded to 2000 mm in the streamwise direction (SUS Co. XAK-P50) and 400 mm in the vertical and spanwise directions, respectively (SUS Co. XA-42L). The output voltage from the hot-wire anemometry was converted to digital data using a data logger (NI USB-6361) and was recorded on a personal computer. The output ports of the controller for the two actuators in the vertical and spanwise directions were connected to the external trigger terminal of the data logger via an in-house circuit, which automates probe traveling and data acquisition.

## *Round and lobed geometries*

To test the diffusion performance of several lobed jets, the geometries of the lobed jets were newly defined. Because each of the geometries in the existing studies was independent, employing the same geometry did not guarantee that it was representative of all lobed geometries, which hinders the generalization of the results obtained.

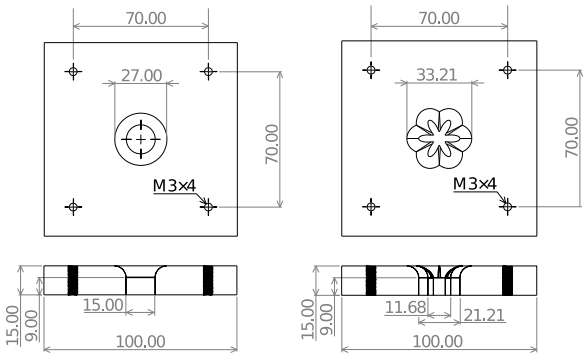


**Figure 5.** Schematic of (left) round nozzle and (right) 6L lobed nozzle (unit: mm).

Therefore, we determined the geometries using a closed polar curve equation containing only two parameters, namely, the number of lobes and the curvature of the lobe peaks. In this study, we tested four types of initial jet conditions: round geometry and three-lobed geometries. However, as mentioned in the introduction, we introduced our own geometry setting. We illustrate the lobed geometries, which are characterized by wavy edges, using a simple sinusoidal curve. Specifically, the geometries of the jet exits

in this study were determined using the following equation:

$$r(\theta) = \frac{D_E}{2}\sqrt{\frac{2b^2}{2b^2+1}}\left(1+\frac{\cos a\theta}{b}\right), \quad (1)$$

where $r$ is the radial direction from the center axis and $\theta$ is the azimuth ($0 \le \theta \le 2\pi$). $D_E$ is the equivalent diameter of the non-circular geometry because the exit area is evaluated $\int r(\theta)^2/2\mathrm{d}\theta = \pi D_E^2/4$. The parameter $a$ (an integer) determines the number of lobes, and $b$ (positive real number) controls the curvature of the lobes. Figure 4 shows the curves produced by Eq. 1 for several sets of parameters. The limit $b \to \infty$ yields a round shape with a radius of $D_E/2$. The three-lobed geometries are referred to as 6L, 6S, and 3L according to their number of lobes $a$ and the curvature (large, $b = 2$; small, $b = 4$).

A schematic of the round and lobed nozzles (only for 6L) is shown in Fig. 5. The nozzles were constructed using acrylic material with dimensions of 100 mm×100 mm×15.00 mm. NC milling was performed to transform the numerical data of the geometries determined using Eq. 1. The (equivalent) diameter of the nozzles, $D_E$, was 15.00 mm. A fillet with a curvature radius of 10.00 mm was formed on the wind tunnel side of the nozzle for the smooth contraction of the jet flow. These nozzles were mounted on the panel of a wind tunnel using four bolts.

### *Experimental conditions*

The origin was set at the center of the jet exit. The coordinate system is Cartesian, $x$ is streamwise, $y$ is vertical, and $z$ is spanwise. The velocity components in the $x$, $y$, and $z$ directions are $\tilde{u}$, $\tilde{v}$, and $\tilde{w}$, respectively. A cylindrical coordinate system and a Cartesian coordinate system can be used owing to the quasi-axisymmetry of the jets. The streamwise direction is $x$ and the radial direction is $r$. For the lobed jets, the radial distributions of the velocity statistics are presented separately for the major (toward lobed peaks) and minor (valleys) axes.

Time averaging was used to evaluate the statistics in the present experiment. The Reynolds decomposition of the instantaneous (streamwise, for example) velocity $\tilde{u}$ is defined by

$$\tilde{u} = U + u, \quad U = \overline{\tilde{u}} = \frac{1}{T}\int_0^T \tilde{u}\mathrm{d}t \ \ (T = N_S/f_S). \quad (2)$$

The number of samples for each measurement location was $N_S = 524,288$ and the sampling frequency was $f_S = 20$ kHz. The jet Reynolds number $Re_J$ is defined as $D_E U_J/\nu$ and set to 70,000, where $U_J$ is the mean streamwise velocity at the jet exit (approximately 70 m/s) and $\nu$ is the kinematic viscosity of air (approximately $1.5 \times 10^{-5}$ m$^2$/s at 25 °C).

The measurements using the I-type hot-wire probe provided the statistics of $u$ over $y-z$ planes. Consequently, the number of measurement trials is $m = 4$ for $U$, $u_{RMS}$ (root-mean-square of $u$; hereafter, referred to as "RMS streamwise velocity"), and $r_{0.5}$ (half width of radial distribution of $U$). The following plots show the average values of the results obtained in the trials.

Figure 6 shows the distribution of the mean streamwise velocity $U$ and the RMS velocity $u_{RMS}$ behind the nozzle. The vertical and horizontal axes, respectively, are normalized by $U_J$ and $D_E$. The distribution of the mean streamwise velocity displays an obvious plateau in the jet core regions for the round jet and in the major and minor axes of the lobed jet. This finding indicates that the upstream conditions in the present study are smooth contraction, which is a typical condition characterized by the *top-hat* distribution of jet ejection. In addition, Fig. 6 also shows that the RMS value of the fluctuating velocity of the jet is less than 3% of the mean velocity. $u_{RMS}/U_J$ in existing studies is represented by 0.9%[8] and 2%[13]. Our results are slightly larger than these; therefore, it can be confirmed that the turbulence was properly suppressed by the wind tunnel equipment.

The streamwise measurement locations for the cross-streamwise velocity statistics distributions were $x/D_E = 2$, 5, 10, 20, and 30. The numbers of the vertical measurement locations were 26 at $x/D_E = 2$ ($0 \le r/r_{0.5} \le 2.5$, where $r_{0.5}$ is half-width of the radial distributions of the mean streamwise velocity) and 31 at $x/D_E \le 5$ ($0 \le r/r_{0.5} \le 3$). The vertical increment of the measurement locations was $0.1r_{0.5}$.

## Experimental results

### *Development characteristics of experimental round and lobed jets*

Figure 7 shows the radial distributions of the mean streamwise velocity $U$ and streamwise RMS velocity $u_{RMS}$ in round and lobed jets obtained at $x/D_E = 2$, 5, 10, 20, and 30. The error bars illustrated together with the plots indicate 95% confidence intervals, that is, twice the standard errors $\pm\sigma/\sqrt{m}$, where $\sigma$ is the (unbiased) standard deviation of the $m = 4$ samples. According to this definition, the confidential intervals converge at the limit of $m \to \infty$, so the error bars never overlap once they are separated from each other. Note that the error bars appear only for the RMS velocity which is more uncertain than the mean velocity. From top to bottom, the results of the round, lobed jet 6L, 6S, and 3L are plotted. The vertical and horizontal axes are normalized by $U_J$ and $D_E$, respectively. For each jet, the diffusion of the mean velocity field is easily confirmed; the mean velocity around the jet centerline decays, and that far from the centerline increases with the $x$. Diffusion of the distribution of $u_{RMS}$ is also seen. The $u_{RMS}$ around the centerline is initially small and the peak of the distribution is located off the centerline but gradually increases, consequently the peak is not outstanding in the large $x$ locations.

The radial distributions of $U$ and $u_{RMS}$ are normalized by the centerline mean streamwise velocity $U_C$ and half-width of the radial distributions of the mean streamwise velocity $r_{0.5}$ to evaluate the asymptotic to the developed self-similarity state (Fig. 8). At $x/D_E = 5$, the radial distributions of $U$ are almost in the self-similarity for all jets. However, the asymptotic to the self-similarity of the radial distributions of $u_{RMS}$ are obviously different according to the initial exit geometries, although self-similarity is confirmed in $x/D_E \ge 20$ for all jets. The development of $u_{RMS}$ in $2 \le x/D_E \le 20$ is the fastest in the round jet, followed by 3L. Meanwhile, the development of $u_{RMS}$ in 6L and 6S is relatively slow and comparable. This implies that the large number of lobes in the initial geometries may

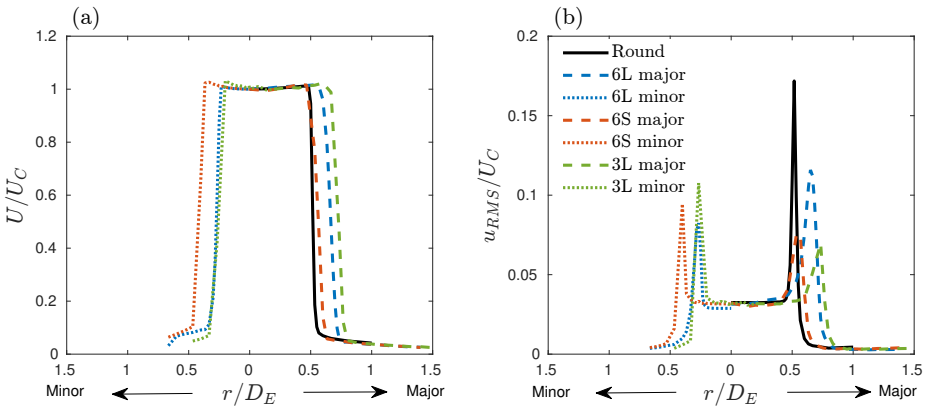


**Figure 6.** (a) Mean streamwise velocity $U$ and (b) RMS of the streamwise fluctuating velocity $u_{RMS}$ behind the nozzle.

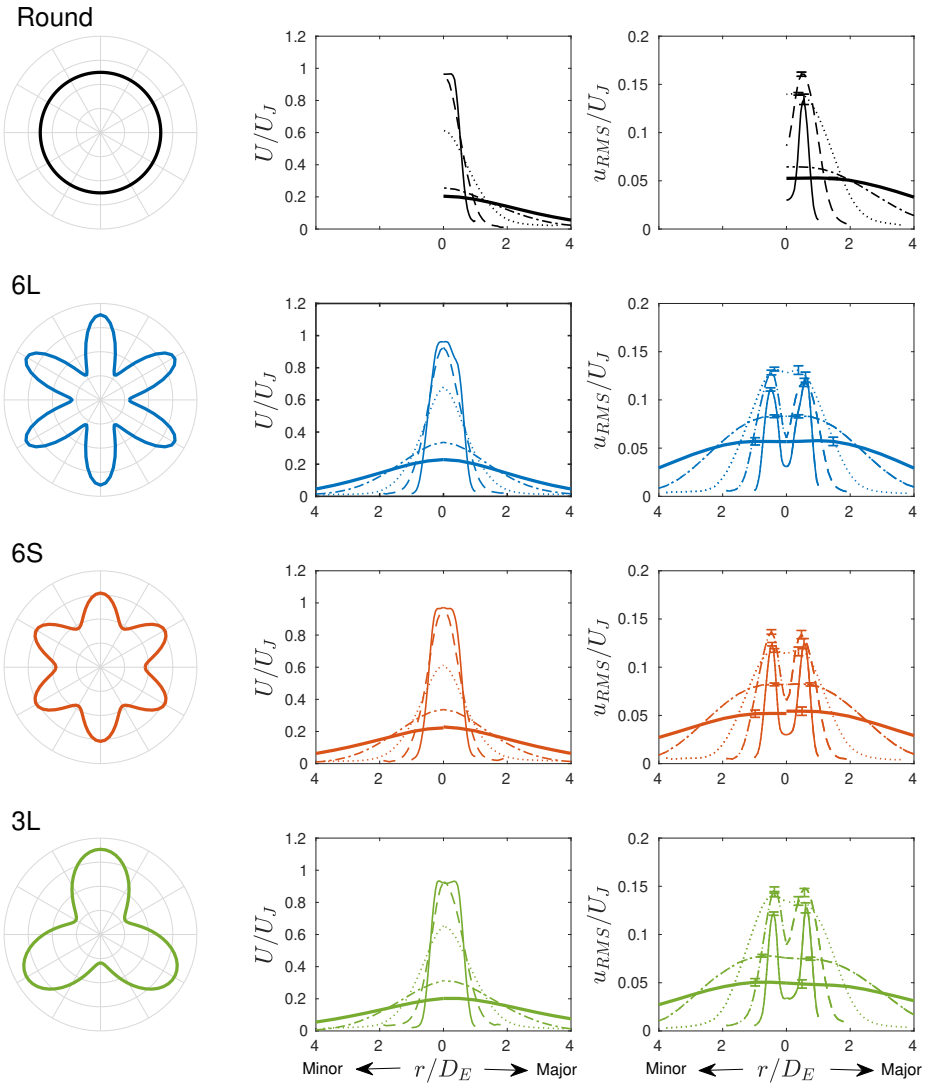


**Figure 7.** Radial distributions of $U$ and $u_{RMS}$ normalized by $U_J$ and $D_E$ at $x/D_E = 2$(thin-solid), $5$(dashed), $10$(dot), $20$(dot-dashed), and $30$(thick-solid). Note that the results along the major (dashed) and minor axes (doted) are shown in the right- and left-half areas of the graphs, respectively. The error bars indicate $95$ confidence intervals of results.

influence the development of the flow field rather than the curvatures of the lobes.

## *Diffusion performance of experimental round and lobed jets*

To quantify the diffusion performance of the jet, the half-width $r_{0.5}$ and centerline mean streamwise velocity $U_C$

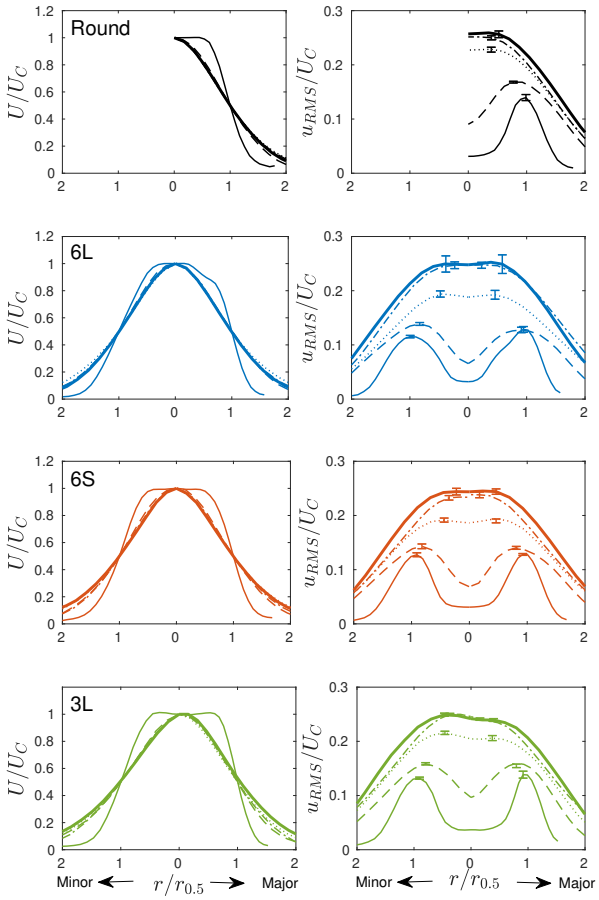


**Figure 8.** The same as Fig. 7, but normalized by $U_C$ and $r_{0.5}$.

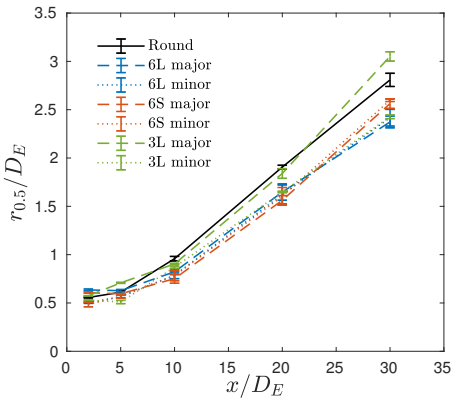


**Figure 9.** Streamwise evolution of $r_{0.5}$s of the jets.

have often been employed in existing studies. In contrast to the development of the flow rate, which has also been evaluated so far, these two quantities are also valid in temporally developing jets as an indication of diffusion performance. Figure 9 shows the streamwise development of half-width $r_{0.5}$. In the developed state, $20 \geq x/D_E$, large $r_{0.5}$s are recorded by the round jet. This indicates that the lobed geometries tend to form a velocity field with smaller diffusion performance in the developed states, even though they were originally developed as diffusion-enhancing techniques. This was already pointed out by Nastase & Meslem[49] who investigated a lobed jet with six lobes. However, the measured velocity field was limited to near the jet exit in their study ($x/D_E \leq 10$), and they did not confirm the asymptotic of the developed states. Only $r_{0.5}$ of lobed jet 3L along the major axis is comparable to that of the round jet. The remaining jets, that is, 6L (both major and minor), 6S (both major and minor), and 3L (minor), are smaller than the two large $r_{0.5}$s. These results indicate an interesting tendency: the mean velocity field is axisymmetric if the number of lobes $a$ is large and non-axisymmetric if $a$ is small. This resembles the results of Ito et al.[54,55] who investigated the diffusion of round jets influenced by half-delta-wing tabs. They demonstrated that if three tabs are installed on the jet exit edge, a non-axisymmetric mean streamwise velocity distribution is achieved. Similar to the lobed exit configurations, the tabs generated streamwise circulating motion in the initial shear layer. Thus, it is expected that the tabs may provide the same controlling effect as lobed jets.

Figure 10 shows the streamwise development of the centerline mean streamwise velocity, $U_C$. The inverse is also plotted to clarify the differences in the developed states. As already confirmed, Fig. 10 shows that the diffusion performance of the lobed jets is inferior to the round jet. Although the error bars of lobed jets 6L and 6S at $x/D_E = 30$ do not overlap with each other, the $U_C$ values of these two jets are comparable. Meanwhile, the $U_C$ of the 3L is between those of the round and 6L (6S) because this jet is non-axisymmetric and has two directions of large and small diffusion along the major and minor axes, respectively. From this result, the diffusion performance of the current jets is concluded to be (round) $>$ (3L) $>$ (6L) $\simeq$ (6S).

## Numerical setups

In this study, the same numerical codes and computer as our previous study[31] were employed for the current simulations. We have already confirmed the current code adequately reproduces the statistical properties of the diffusing round jet field, such as radial distributions of the mean streamwise velocity, RMS of fluctuating velocity, and Reynolds shear stress, at varying initial $Re_J$s (70, 000, 40, 000, and 10, 000).

The overview of the simulations can be obtained in a movie, showing the temporal development of instantaneous streamwise velocity and vortex structures (illustrated by $Q$, defined later). The numerical code was based on "DNSLab"[56], a Navier–Stokes solver that consists of pseudospectral scripts for spatial numerical derivatives, a fourth-order Runge–Kutta scheme for temporal increments, and de-aliasing using the 2/3 rule. Although the original code was written for a two-dimensional flow in a periodic square, it can easily be modified for a three-dimensional flow in a periodic cube. Furthermore, we added the subgrid-scale (SGS) stress model for the LES simulation.

Then, the instantaneous velocity $(\tilde{u}, \tilde{v}, \tilde{w})$ is now the filtered velocity in the current study, following the governing equations of the Navier–Stokes equations and the continuity equation for the grid-scale velocity field (hereafter, all variables are normalized by $U_J$ and $D_E$ unless otherwise

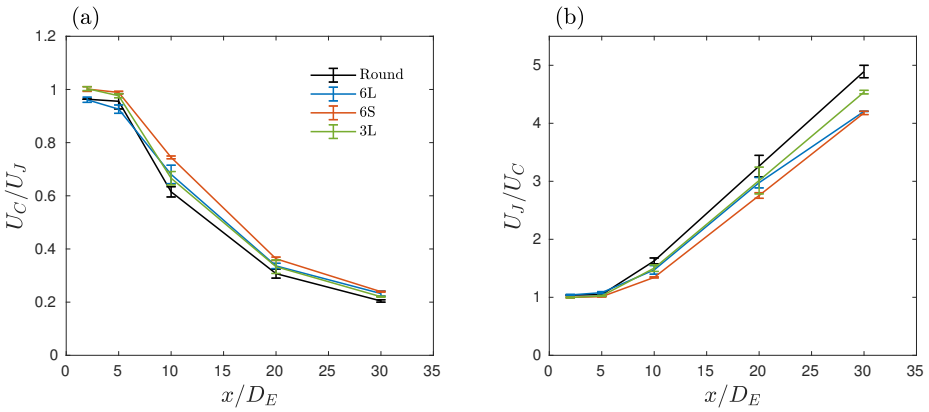


**Figure 10.** Streamwise development of $U_C$s of the jets (a) and the inverse plots (b).

noted):

$$\frac{\partial \tilde{u}_i}{\partial t} + \tilde{u}_j \frac{\partial \tilde{u}_i}{\partial x_j} = -\frac{\partial \tilde{p}}{\partial x_i} + \frac{1}{Re_J}\frac{\partial^2 \tilde{u}_i}{\partial x_j \partial x_j} - \frac{\partial \tau_{ij}}{\partial x_j}, \quad (3)$$

$$\frac{\partial \tilde{u}_i}{\partial x_i} = 0, \quad (4)$$

where $p$ is the static pressure per unit mass and $\tau_{ij}$ is the sub-grid-scale (SGS) stress.

In the pseudospectral (co-location) method, owing to the homogeneity and periodicity of the flow field, we can evaluate the derivative of the velocity using the Fourier transform. The nonlinear, viscous, and SGS stress terms are respectively evaluated as follows:

$$\tilde{u}_j \frac{\partial \tilde{u}_i}{\partial x_j} = \tilde{u}_j \mathcal{F}^{-1}(\imath k_j \mathcal{F}(\tilde{u}_i)), \quad (5)$$

$$\frac{1}{Re_J}\frac{\partial^2 \tilde{u}_i}{\partial x_j \partial x_j} = \frac{1}{Re_J}\mathcal{F}^{-1}(-k_j^2 \mathcal{F}(\tilde{u}_i)), \quad (6)$$

$$\frac{\partial \tau_{ij}}{\partial x_j} = \mathcal{F}^{-1}(\imath k_j \mathcal{F}(\tau_{ij})), \quad (7)$$

where $\imath$ is the imaginary unit. This scheme eliminates the truncation error of the velocity derivative components caused by the finite difference approximation. Furthermore, the pressure $\tilde{p}$ is not explicitly evaluated in the pseudospectral method; instead, we use the orthogonality between the Fourier coefficients of velocity and the wavenumber vector, which is given by the Fourier transform of Eq. 4,

$$\mathcal{F}\left(\frac{\partial \tilde{u}_i}{\partial x_i}\right) = \imath k_i \mathcal{F}(\tilde{u}_i). \quad (8)$$

Projecting the Fourier coefficient onto the wavenumber vector, we obtain the component parallel to the wavenumber vector,

$$k_i \frac{k_j \mathcal{F}(\tilde{u}_j)}{k_k^2}. \quad (9)$$

Therefore, the divergence-free velocity field can be obtained as follows, without evaluating the pressure field,

$$\mathcal{F}^{-1}\left(\mathcal{F}(\tilde{u}_i) - k_i \frac{k_j \mathcal{F}(\tilde{u}_j)}{k_k^2}\right). \quad (10)$$

The SGS stress is modeled in the present LES using the Smagorinsky model, which yields

$$\tau_{ij} = -2C\Delta^2 \sqrt{2S_{kl}\,S_{kl}}\,S_{ij}, \quad (11)$$

where $\Delta$ is the filter width (equivalent to the grid space, which is uniform in this study), $S_{ij} = (1/2)(\partial \tilde{u}_i/\partial x_j + \partial \tilde{u}_j/\partial x_i)$ is the rate-of-strain tensor. We employed a dynamically determined model coefficient $C$ based on the detection of relatively small-scale eddies[57],

$$C = \frac{1}{20}|F|^{3/2}, \quad (12)$$

where, letting $W_{ij} = (1/2)(\partial \tilde{u}_i/\partial x_j - \partial \tilde{u}_j/\partial x_i)$ as the rate-of-rotation tensor,

$$F \equiv \frac{Q}{E}, \quad (13)$$

$$Q = \frac{1}{2}\left(W_{ij}\,W_{ij} - S_{ij}\,S_{ij}\right),\ E = \frac{1}{2}\left(W_{ij}\,W_{ij} + S_{ij}\,S_{ij}\right).$$

This model coefficient is always positive and thus numerically stable. Furthermore, this model is plausible in the sense that the forward energy cascade (i.e., energy transfer from larger to smaller scale motions) is localized around the eddy structures.

Both Cartesian and cylindrical coordinate systems whose definition is the same as the experiments were employed in the simulations. The numerical domain sizes along the $x$, $y$, and $z$ directions were $(L_x, L_y, L_z) = (8\pi D, 4\pi D, 4\pi D)$. The number of grid points is $(N_x, N_y, N_z) = (512, 256, 256)$. As described in the following, the initial conditions are aimed at reproducing those in the experimental jets. In the initial state, a column-like high-speed region is embedded in the numerical domain; $u(y, z) = U_J$ for $r \leq D_E/2$ in Eq. 1 and 0 elsewhere. The initial jet Reynolds numbers $Re_J$ were $D_E U_J/\nu = 70,000$, where $\nu$ is the kinematic viscosity of the fluid. All three components in the initial jet cores were disturbed by uniformly distributed random numbers with a root-mean-square value of $0.03U_J$. The simulation time was $0 \leq t \leq 25$, and the time increment $\Delta t$ was set to 0.01 such that the Courant–Friedrichs–Lewy condition $U_J \Delta t < \Delta x$ $(\equiv L_x/N_x)$ was satisfied. The instantaneous, three-dimensional flow data were recorded for storage in our computer every $10\Delta t$; therefore, we obtained 250 datasets.

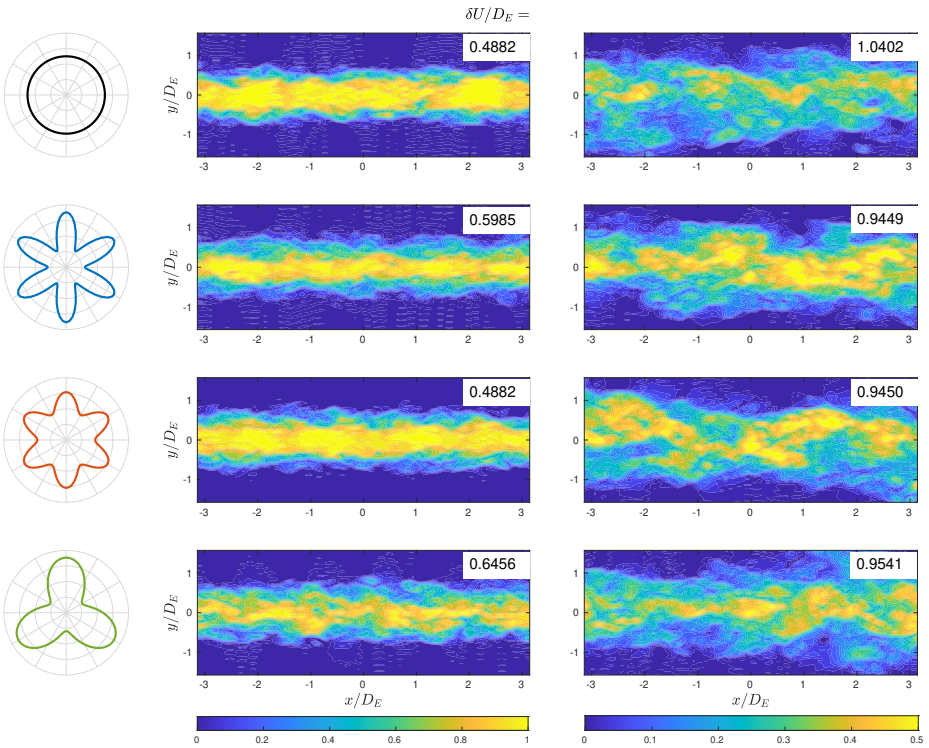


**Figure 11.** Contours of instantaneous streamwise velocity over $x-y(z=0)$ plane at $t=5$ and 20.

## Numerical results

### *Development characteristics of numerical round and lobed jets*

Figure 11 shows the instantaneous velocity field over $x-y$ plane crossing the jet core. The velocity fields at $t=5$ and 20 are shown for the earlier and later stages, respectively. Using this figure, we check the qualitative diffusion performance from the viewpoint of the shear layer thickness. At $t=5$, the shear layer of the lobed jet 6L is the thickest, followed by the 3L and 6S, and that of the round jet is the thinnest. As seen in this figure, the lobed jets in the present simulations diffuse faster than the round jets, acting as a diffusion-enhancing technique in developing states. The share layer thickness is quantified as

$$\delta_U \equiv r|_{U=0.1U_C} - r|_{U=0.9U_C}. \tag{14}$$

The shear layer thickness along the major axis for each jet is indicated at the top-right corner of the velocity map, showing the superior diffusion performance of the lobed jets with the large lobes (6L and 3L) at the earlier stages.

At $t=20$, however, we discovered that the area of the high-speed region ($u/U_J > 0.5$, indicated by the yellow color) of the round jet is seen to be thinner than those of the lobed jets. This implies a lower diffusion performance of the simulated lobed jets in the developed states. Indeed, the shear layer thickness of the lobed jet 6L is smaller than that of the round jet. The largest diffusion of the round jet is followed by the 3L, but the departure from the 6L and 6S is not large ($\sim 1\%$). The results of 6L and 6S are comparable, which is consistent with what we have seen in the experimental results.

Figure 11 shows the development of the radial distributions of the mean streamwise velocity $U$ and the RMS of the streamwise fluctuating velocity $u_{RMS}$. The results around the centerline are not illustrated because they are distorted by the coordinate transformation of the data from Cartesian to cylindrical shapes. As jet flows are statistically unsteady processes, we employ the spatial average in two homogeneous directions (streamwise and azimuthal). For example, the Reynolds decomposition of the instantaneous velocity $u$ is given by

$$\tilde{u} = U + u', \;\; U = \langle \tilde{u} \rangle = \frac{1}{8\pi}\frac{1}{a}\int_{-4\pi}^{4\pi}\sum_{i}^{a}\tilde{u}_i \mathrm{d}x, \tag{15}$$

where $\tilde{u}_i$ denotes the radial distribution of the instantaneous velocity $\tilde{u}$ along the $i$th major (or minor) axis of the lobed jets. For a round jet, this summation is reduced to integration in the azimuthal direction. Although we can evaluate a greater variety of statistics using numerical data, only these two quantities can be compared with experimental results. It is illustrated that the mean velocity $U$ is almost self-similar at $t \geq 5$ for all four jet cases. Meanwhile, the graphs of $u_{RMS}$ show much clearer different development characteristics. $u_{RMS}$ of the round jet is self-similar at $t \geq 15$, which is faster than that of any lobed jet. The self-similarity distributions of lobed jets 6S and 3L were confirmed for $t \geq 20$. Such a slower asymptotic to the self-similarity is confirmed in the experimental results. The self-similarity of the 6L is not confirmed in this study, but the asymptotic distribution must be close to the results at $t \gtrsim 20$.

### *Diffusion performance of numerical round and lobed jets*

As well as the experimental results, the diffusion performance of the simulated jets is quantified using the half-width

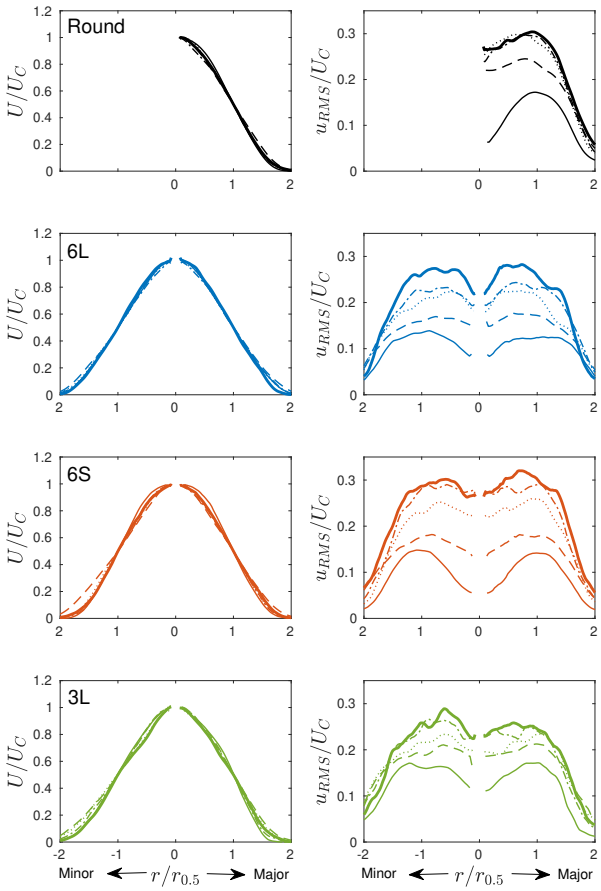


**Figure 12.** Radial distributions of $U$ and $u_{RMS}$ normalized by $U_C$ and $r_{0.5}$ at $t = 5$(thin-solid), 10(dashed), 15(dot), 20(dot-dashed), and 25(thick-solid). Note that the results along the major (dashed) and minor axes (doted) are shown in the right- and left-half areas of the graphs, respectively.

$r_{0.5}$ and the centerline mean streamwise velocity$U_C$. Figure 13 shows the temporal development of the $r_{0.5}$s and the $U_C$s of four jets. The curves of half-width $r_{0.5}$ in Fig. 13 (a) display the inferior diffusion performance of the three-lobed jets to the round jets in the developed states. Specifically, the largest is the round, which is comparable to the 3L along the major axis. However, the $r_{0.5}$ of the 3L along the minor axis is much smaller, thus the diffusion of 3L can be concluded to be smaller than the round jet. The $r_{0.5}$s of the 6L along both the major and minor axes are as small as the 3L along the minor axis, indicating the smallest diffusion performance of 6L in the developed states. While the lobed jets 6L and 6S are axisymmetric after the disappearance of the potential cores, 3L is never axisymmetric. The above characteristics are in excellent agreement with the experimental results. The only difference is that the $r_{0.5}$s of the 6S is larger than those of 6L in $t \gtrsim 17$, but comparable with each other in $5 \lesssim t \lesssim 17$.

The differences in $U_C$ curves in Fig. 13 (b) are clearer than the experimental results. The earlier disappearance of the potential core ($U_C/U_J = 1.0$) of the lobed jets 6L and 3L compared to that of the round jet indicates the diffusion enhancement of these two configurations in the early stages. However, after the disappearance of the potential core, the decay of $U_C$ of the round jet is greater than that of the other lobed jets. We find that the result of 6S is not between that of the round and 6L only for this figure, but the reason remains unknown. Meanwhile, the decay of $U_C$ in the developing states ($5 \lesssim t^* \lesssim 10$) did not agree with the experimental results; the decay of the 6L and 3L jets is faster than the round jet. Therefore, the consistency of the diffusion performance between the temporally and spatially developing flows is limited in the fully developed states. This is further discussed in the following section.

By plotting $U_C$ of the round jet on the logarithmic axis, we confirm that the decay of $U_C$ is approximated as $t^{-1}$ (not presented). Based on the constraint of flow-rate conservation, $r_{0.5}$ of the round jet may be approximated as $t^{1/2}$. Instead of time $t$, we can define "traveling distance" as,

$$x_T(t) \equiv \int_0^t U_C \mathrm{d}t. \tag{16}$$

By plotting $r_{0.5}$s as functions of $x_T$, as in Fig. 14, we find approximately linear developments of $r_{0.5}$ of the round jet, similar to those in the spatially developing jets. This also shows the diffusion performance of the current four jets and their consistency with the experimental results (Fig. 9) clearer than Fig. 13 (a). However, if so, $U_C \propto x_T^{-2}$ which is not the scaling of the spatially developing jets. Consequently, the comparison between spatially and temporally developing jets is limited to qualitative discussions.

## Discussions

Although limited to a qualitative discussion, the attempt to reproduce the diffusion performance of laboratory jets and its exit geometry dependence using the LESs of temporally developing jets is quite successful. For further application of the simulations of temporally developing flows, it is better to consider why temporally developing jets provide a diffusion performance similar to that of spatially developing jets.

As described above, the flow rate of spatially developing jets monotonically increases with the streamwise distance $x$ whereas that of temporally developing jets is conserved. This was caused by differences in the boundary conditions. In spatially developing jets, the radial mean velocity $V$ is finite and is derived from the continuity equation, which increases the flow rate. In temporally developing jets, because of the streamwise homogeneity $\partial U/\partial x = 0$, $V_r$ at the lateral boundaries is zero. Consequently, the field of the vertical mean velocity in temporally developing jets departs from that in spatially developing jets.

This can be easily confirmed by checking the mean velocity field in lobed jet 6L in the earlier stage, which has been visualized in many experimental studies. Figure 15 (a) shows the arrows of the mean cross-streamwise velocity $\mathbf{v_r}$ over the $Y - Z$ plane at $t = 2.5$ together with the contour of the mean streamwise velocity $U$. At this time, the potential core remains and $U$ is distributed according to the jet exit geometry. A pair of counter-rotating streamwise vortices is observed at each peak of the lobed geometry. Owing to this swirling motion, the flow is inward along the major axis and outward along the minor axis. However, as shown in Fig. 15 (b) shows the schematic of the mean flow field just behind the lobed jet exit, observed in several experimental studies on the lobed jets with 6 peaks[48,49,51,53].

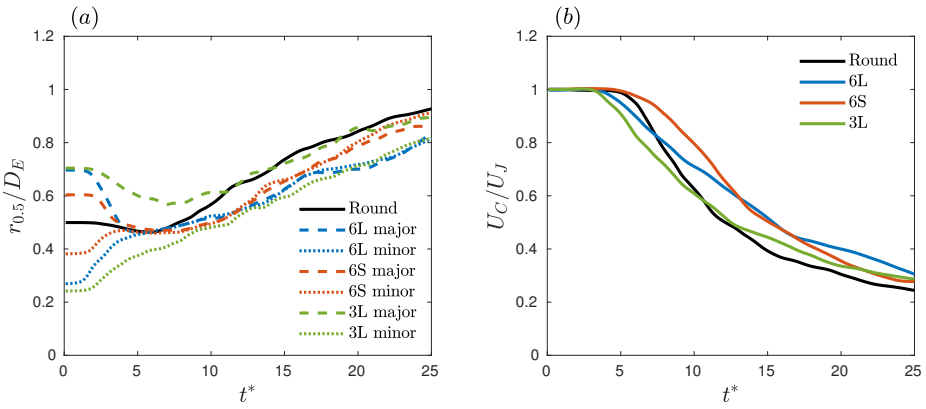


**Figure 13.** Temporal evolution of (a) $r_{0.5}$s and (b) $U_C$s of the jets.

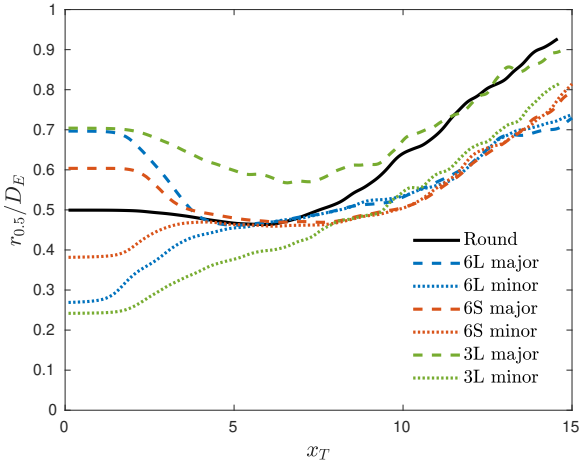


**Figure 14.** Temporal evolution of $r_{0.5}$s versus $x_T$.

This illustration also indicates pairs of symmetrical counter-rotating streamwise vortices across the lobe peaks; however, note that the directions of rotation are opposite to those in Fig. 15 (a). These counter-rotating streamwise vortices are widely believed to be important for diffusion enhancement in lobed jets, but cannot be reproduced by the present simulations. This result indicates that we should not use simulations of temporally developing jets to investigate the jet flow structures in the earlier stages, where the mean cross-streamwise velocity field plays an important role. The reason the diffusion of the jets in the developing states contradicts the temporally and spatially developing flows might be caused by such a discrepancy in the swirling motions.

In the developed field, however, the mean cross-streamwise velocity is almost independent of jet diffusion: the diffusion of $U$ is exclusively carried by turbulence. Furthermore, the production of turbulence is the interaction between the mean velocity gradient and turbulence, and the leading term is not $\partial V_r/\partial r$ but $\partial U/\partial r$. Therefore, the difference in the mean cross-streamwise velocity fields was not crucial. The remaining possibility is that the turbulent structures that diffuse through the mean streamwise velocity are similar in both temporally and spatially developing jets. Indeed, In our previous work on the temporally developing round jet, we have identified a large-scale helical structure that also has been observed experimentally[31].

These results provide two interesting suggestions. First, simulations of temporally developing jets are useful for investigating three-dimensional turbulence structures. The structures in temporally developing jets are a good model for spatially developing jets in laboratory experiments. Owing to streamwise homogeneity, we can employ several modal analysis techniques to detect the dominant flow structures, as in our previous work. Furthermore, the flow never exits the numerical domain because of the periodicity, and we can track the evolution of the structures over a sufficiently long time. Second, the mean cross-streamwise velocity and its swirling motions are important for the lobed jets in the earlier stages but do not affect the turbulence structures in the developed state and their evolution. Many researchers who know the lobed jets well may be interested in how the streamwise vortices, as depicted in (b), evolve into turbulence structures in the developed states that determine the diffusion performance. However, note that these vortices are mean velocity components and are independent of the diffusion of $U$.

## Conclusions

This study aimed to reproduce the diffusion performance of lobed jets using numerical simulations of temporally developing flows. The diffusion performance of a round jet and three-lobed jets with different numbers and curvatures of lobes (6L, 6S, and 3L) were tested in both wind tunnel experiments and numerical simulations.

In the experiments, the velocity fields of the four jets were formed in a wind tunnel and measured using a hot-wire anemometer. The self-similarity of the flow field was confirmed by the radial distribution of the mean streamwise velocity and RMS streamwise velocity. The diffusion performances of the jets in the fully developed state were evaluated and compared. From the half-width and centerline mean streamwise velocity in the fully developed state, we conclude that the largest diffusion performance is recorded by the round jet, which is followed by 3L, while 6L and 6S are the smallest and are comparable with each other. Specifically, the half-width of (a) round and 3L (along the major axes) are comparable, (b) 3L was non-axisymmetric whole over the flow field and thus the diffusion performance of 3L is inferior to the round jet, (c) 6L and 6S are comparable, indicating that these jet flows are almost

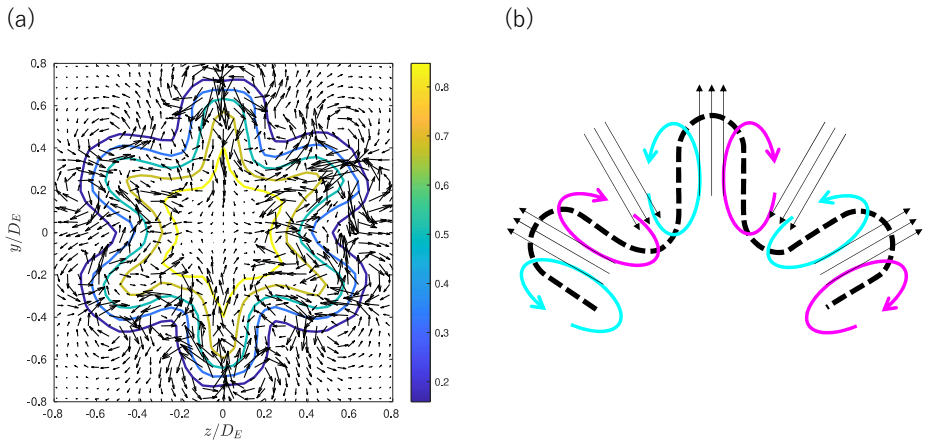


**Figure 15.** (a) Arrows of mean cross-streamwise velocity $\mathbf{v_r}$ over the $Y-Z$ plane at $t=2.5$ together with the contour of mean streamwise velocity $U$ and (b) schematic of the mean flow field behind the lobed jet exit, observed in several experimental studies on the lobed jets with 6 peaks.

axisymmetric, and finally, (d) 3L (along the minor axes) is comparable with 6L and 6S. The diffusion performance of 6L and 6S jets is smaller than the others (actually, this feature is less clear than the above three).

In the numerical simulations, the velocity fields of the four jets were simulated using the LESs of temporally developing flows, and the diffusion performance of the jets was compared with those in the experiments. The diffusion performance of the jets was evaluated again using the half-width and centerline mean streamwise velocity in $t^* \gtrsim 20$, and the results were found to be in good agreement with the above-mentioned experimental results. In particular, the half-width graph with traveling distance $x_T$ on the horizontal axis was in excellent agreement with the experimental results. The mechanism for this consistency is considered to be the turbulent structures contributing to the mean velocity diffusion.

In summary, this study demonstrated that the simulations of temporally developing flows can generate round and lobed jets with similar diffusion performance to the spatially developing flows. From the results, we propose that temporally developing jets are very good models of those generated in wind tunnel experiments. Our investigation was limited to the diffusion of the lobed jets, but we expect that the influence of any type of initial conditions on the jet development, including exit geometries and initial mean velocity distributions, can be reproduced in the temporally developing flow simulations. This potential helps our future investigations of the turbulence structures in the flow fields owing to their streamwise homogeneity.

### Acknowledgements

The authors are grateful to Mr. Komei Fujikura and Mr. Toru Mukai for their help in the experiments. We also thank Toshihiko Shakouch, Ph.D. for valuable discussions.

## Declaration of conflicting interests

The authors declared no potential conflicts of interest.

## Funding

This study was financially supported by the Okasan-Kato Foundation, Maeda Engineering Foundation, and JSPS Grants-in-Aid for Scientific Research (22K14179).

## ORCID ID

Mamoru Takahashi 0000-0001-8773-264X

## Data availability

The experimental/numerical data and data analysis programs can be available if requested.

### References

1. George WK. Asymptotic effect of initial and upstream conditions on turbulence. *Journal of fluids engineering* 2012; 134(6): 061203. DOI:10.1115/1.4006561.
2. Bevilaqua PM and Lykoudis PS. Turbulence memory in self-preserving wakes. *Journal of fluid mechanics* 1978; 89(3): 589–606. DOI:10.1017/S002211207800275X.
3. Wygnanski I, Champagne F and Marasli B. On the large-scale structures in two-dimensional, small-deficit, turbulent wakes. *Journal of fluid mechanics* 1986; 168: 31–71. DOI: 10.1017/S0022112086000289.
4. Cannon S, Champagne F and Glezer A. Observations of large-scale structures in wakes behind axisymmetric bodies. *Experiments in fluids* 1993; 14(6): 447–450. DOI:10.1007/BF00190199.
5. Mi J, Nathan GJ and Nobes DS. Mixing characteristics of axisymmetric free jets from a contoured nozzle, an orifice plate and a pipe. *Journal of fluids engineering* 2001; 123(4): 878–883. DOI:10.1115/1.1412460.
6. Xu G and Antonia R. Effect of different initial conditions on a turbulent round free jet. *Experiments in fluids* 2002; 33(5): 677–683. DOI:10.1007/s00348-002-0523-7.
7. Mi J, Kalt P, Nathan GJ et al. PIV measurements of a turbulent jet issuing from round sharp-edged plate. *Experiments in fluids* 2007; 42(4): 625–637. DOI:10.1007/s00348-007-0271-9.
8. Duffet JC and Benaïssa A. Influence of initial conditions on the evolution towards similarity of passive scalar in turbulent

round jets. *Experimental Thermal and Fluid Science* 2013; 44: 834–843. DOI:10.1016/j.expthermflusci.2012.09.029.
9. Laban A, Aleyasin SS, Tachie MF et al. Experimental investigation of nozzle spacing effects on characteristics of round twin free jets. *Journal of fluids engineering* 2019; 141(7): 071201. DOI:10.1115/1.4041989.
10. Morris EM, Aleyasin SS, Biswas N et al. Turbulent properties of triple elliptic free jets with various nozzle orientation. *Journal of fluids engineering* 2020; 142(3): 031106. DOI: 10.1115/1.4045619.
11. Mi J and Nathan GJ. Statistical properties of turbulent free jets issuing from nine Differently-Shaped nozzles. *Flow, Turbulence and Combustion* 2010; 84(4): 583–606. DOI: 10.1007/s10494-009-9240-0.
12. Hashiehbaf A and Romano GP. Particle image velocimetry investigation on mixing enhancement of non-circular sharp edge nozzles. *International Journal of Heat and Fluid Flow* 2013; 44: 208–221. DOI:10.1016/j.ijheatfluidflow.2013.05.017.
13. Aleyasin SS, Tachie MF and Koupriyanov M. PIV measurements in the near and intermediate field regions of jets issuing from eight different nozzle geometries. *Flow, Turbulence and Combustion* 2017; 99(2): 329–351. DOI: 10.1007/s10494-017-9820-3.
14. Aleyasin SS, Tachie MF and Koupriyanov M. Statistical properties of round, square, and elliptic jets at low and moderate reynolds numbers. *Journal of fluids engineering* 2017; 139(10): 101206. DOI:10.1115/1.4036824.
15. Aleyasin SS, Fathi N, Tachie MF et al. On the development of incompressible round and equilateral triangular jets due to reynolds number variation. *Journal of fluids engineering* 2018; 140(11): 111202. DOI:10.1115/1.4040031.
16. Morris EM, Biswas N, Aleyasin SS et al. Particle image velocimetry measurements of turbulent jets issuing from twin elliptic nozzles with various orientations. *Journal of fluids engineering* 2020; 143(2): 021501. DOI:10.1115/1.4048684.
17. Kristo PJ, Hoff CD, Craig IGR et al. Turbulent mixing process of a round jet with slot lobes. *Journal of fluids engineering* 2020; 143(3): 031502. DOI:10.1115/1.4049059.
18. Antonia RA, Chambers AJ, Britz D et al. Organized structures in a turbulent plane jet: topology and contribution to momentum and heat transport. *Journal of fluid mechanics* 1986; 172: 211–229. DOI:10.1017/S0022112086001714.
19. Gordeyev SV and Thomas FO. Coherent structure in the turbulent planar jet. part 1. extraction of proper orthogonal decomposition eigenmodes and their self-similarity. *Journal of fluid mechanics* 2000; 414: 145–194. DOI:10.1017/S002211200000848X.
20. Gordeyev SV and Thomas FO. Coherent structure in the turbulent planar jet. part 2. structural topology via POD eigenmode projection. *Journal of fluid mechanics* 2002; 460: 349–380. DOI:10.1017/S0022112002008364.
21. Tanaka N, Sakai Y, Yamamoto M et al. On the development of coherent structure in a plane jet: Part 4, the multipoint simultaneous measurement of Two-Component velocities and the simple coherent structure model. *JSME International Journal Series B: Fluids and Thermal Engineering* 2006; 49(4): 899–905. DOI:10.1299/jsmeb.49.899.
22. Terashima O, Sakai Y, Goto Y et al. On the turbulent energy transport related to the coherent structures in a planar jet. *Experimental Thermal and Fluid Science* 2015; 68: 697–710. DOI:10.1016/j.expthermflusci.2015.07.009.
23. Takahashi M, Iwano K, Sakai Y et al. Three-dimensional visualization of destruction events of turbulent momentum transfer in a plane jet. *Physics of fluids* 2019; 31(10): 105114. DOI:10.1063/1.5122219.
24. Dimotakis PE, Miake-Lye RC and Papantoniou DA. Structure and dynamics of round turbulent jets. *Physics of fluids* 1983; 26(11): 3185–3192. DOI:10.1063/1.864090.
25. Tso J and Hussain F. Organized motions in a fully developed turbulent axisymmetric jet. *Journal of fluid mechanics* 1989; 203: 425–448. DOI:10.1017/S0022112089001539.
26. Gamard S, George WK, Jung D et al. Application of a "slice" proper orthogonal decomposition to the far field of an axisymmetric turbulent jet. *Physics of fluids* 2002; 14(7): 2515–2522. DOI:10.1063/1.1471875.
27. Gamard S, Jung D and George WK. Downstream evolution of the most energetic modes in a turbulent axisymmetric jet at high reynolds number. part 2. the far-field region. *Journal of fluid mechanics* 2004; 514: 205–230. DOI:10.1017/S0022112004000175.
28. Mullyadzhanov RI, Sandberg RD, Abdurakipov SS et al. Propagating helical waves as a building block of round turbulent jets. *Physical Review Fluids* 2018; 3(6): 062601. DOI:10.1103/PhysRevFluids.3.062601.
29. Samie M, Lavoie P and Pollard A. Quantifying eddy structures and very-large-scale motions in turbulent round jets. *Journal of fluid mechanics* 2021; 916: A2. DOI:10.1017/jfm.2021.183.
30. Samie M, Aparece-Scutariu V, Lavoie P et al. Three-dimensional large-scale and very-large-scale coherent structures in a turbulent axisymmetric jet. *Journal of fluid mechanics* 2022; 948: A29. DOI:10.1017/jfm.2022.703.
31. Takahashi M, Fukui R, Tsujimoto K et al. Helical structures in a temporally developing round jet in the developed state. *Flow, Turbulence and Combustion* 2023; 111(1): 59–79. DOI: 10.1007/s10494-023-00423-4.
32. da Silva CB and Pereira JCF. Invariants of the velocity-gradient, rate-of-strain, and rate-of-rotation tensors across the turbulent/nonturbulent interface in jets. *Physics of fluids* 2008; 20(5): 055101. DOI:10.1063/1.2912513.
33. Hawkes ER, Chatakonda O, Kolla H et al. A petascale direct numerical simulation study of the modelling of flame wrinkling for large-eddy simulations in intense turbulence. *Combustion and Flame* 2012; 159(8): 2690–2703. DOI:10.1016/j.combustflame.2011.11.020.
34. Yang Y, Wang H, Pope SB et al. Large-eddy simulation/probability density function modeling of a non-premixed CO/H2 temporally evolving jet flame. *Proceedings of the Combustion Institute* 2013; 34(1): 1241–1249. DOI:10.1016/j.proci.2012.08.015.
35. Taveira RR and da Silva CB. Kinetic energy budgets near the turbulent/nonturbulent interface in jets. *Physics of fluids* 2013; 25(1): 015114. DOI:10.1063/1.4776780.
36. van Reeuwijk M and Holzner M. The turbulence boundary of a temporal jet. *Journal of fluid mechanics* 2014; 739: 254–275. DOI:10.1017/jfm.2013.613.
37. Nagata R, Watanabe T and Nagata K. Turbulent/non-turbulent interfaces in temporally evolving compressible planar jets. *Physics of fluids* 2018; 30(10). DOI:10.1063/1.5047395.
38. Bogey C and Pineau P. Potential-core closing of temporally developing jets at mach numbers between 0.3 and 2: Scaling and conditional averaging of flow and sound fields.

*Physical Review Fluids* 2019; 4(12): 124601. DOI:10.1103/PhysRevFluids.4.124601.

39. Pineau P and Bogey C. Temperature effects on convection speed and steepened waves of temporally developing supersonic jets. *AIAA Journal* 2020; 58(3): 1227–1239. DOI: 10.2514/1.J058589.
40. Shamooni A, Cuoci A, Faravelli T et al. An a priori DNS analysis of scale similarity based combustion models for LES of non-premixed jet flames. *Flow, Turbulence and Combustion* 2020; 104(2): 605–624. DOI:10.1007/s10494-019-00099-9.
41. Hayashi M, Watanabe T and Nagata K. The relation between shearing motions and the turbulent/non-turbulent interface in a turbulent planar jet. *Physics of fluids* 2021; 33: 055126. DOI: 10.1063/5.0045376.
42. Moser RD, Rogers MM and Ewing DW. Self-similarity of time-evolving plane wakes. *Journal of fluid mechanics* 1998; 367: 255–289. DOI:10.1017/S0022112098001426.
43. Rogers MM and Moser RD. Direct simulation of a self-similar turbulent mixing layer. *Physics of fluids* 1994; 6(2): 903–923. DOI:10.1063/1.868325.
44. Watanabe T, Zhang X and Nagata K. Direct numerical simulation of incompressible turbulent boundary layers and planar jets at high Reynolds numbers initialized with implicit large eddy simulation. *Computers & fluids* 2019; 194: 104314. DOI:10.1016/j.compfluid.2019.104314.
45. Kozul M, Jason Hearst R, Monty JP et al. Response of the temporal turbulent boundary layer to decaying free-stream turbulence. *Journal of fluid mechanics* 2020; 896: A11. DOI: 10.1017/jfm.2020.320.
46. Hu H, Kobayashi T, Saga T et al. Particle image velocimetry and planar laser-induced fluorescence measurements on lobed jet mixing flows. *Experiments in fluids* 2000; 29(1): S141–S157. DOI:10.1007/s003480070016.
47. Hu H, Saga T, Kobayashi T et al. A study on a lobed jet mixing flow by using stereoscopic particle image velocimetry technique. *Physics of fluids* 2001; 13(11): 3425–3441. DOI: 10.1063/1.1409537.
48. Hu H, Saga T, Kobayashi T et al. Mixing process in a lobed jet flow. *AIAA journal* 2002; 40: 1339–1345. DOI: 10.2514/3.15201.
49. Nastase I and Meslem A. Vortex dynamics and mass entrainment in turbulent lobed jets with and without lobe deflection angles. *Experiments in fluids* 2010; 48(4): 693–714. DOI:10.1007/s00348-009-0762-y.
50. Nastase I, Meslem A and El Hassan M. Image processing analysis of vortex dynamics of lobed jets from three-dimensional diffusers. *Fluid dynamics research* 2011; 43(6): 065502. DOI:10.1088/0169-5983/43/6/065502.
51. Shakouchi T, Iriyama S, Kawashima Y et al. Flow characteristics of submerged free jet flow from petal-shaped nozzle. *Journal of fluid science and technology* 2014; 9(3): JFST0037–JFST0037. DOI:10.1299/jfst.2014jfst0037.
52. Sheng ZQ, Yao Y and Xu YH. Suggestions on investigations of lobed jet mixing. *Aerospace Science and Technology* 2019; 86: 415–429. DOI:10.1016/j.ast.2019.01.042.
53. Sheng ZQ, Liu JY, Yao Y et al. Mechanisms of lobed jet mixing: About circularly alternating-lobe mixers. *Aerospace Science and Technology* 2020; 98: 105660. DOI:10.1016/j.ast.2019.105660.
54. Ito Y, Miura K, Sakai Y et al. Enhancement and suppression of mixing and diffusion in an axisymmetric jet by half delta-wing tabs. *International journal of heat and mass transfer* 2018; 118: 1218–1230. DOI:10.1016/j.ijheatmasstransfer.2017.11.053.
55. Ito Y, Naganawa K, Sakai Y et al. Momentum diffusion near jet exit in a round jet controlled by half Delta-Wing tabs. *Flow, Turbulence and Combustion* 2020; 105(3): 715–734. DOI: 10.1007/s10494-020-00129-x.
56. Vuorinen V and Keskinen K. DNSLab: A gateway to turbulent flow simulation in matlab. *Computer physics communications* 2016; 203: 278–289. DOI:10.1016/j.cpc.2016.02.023.
57. Kobayashi H. The subgrid-scale models based on coherent structures for rotating homogeneous turbulence and turbulent channel flow. *Physics of fluids* 2005; 17(4): 045104. DOI: 10.1063/1.1874212.
58. Hussain, Fazle and Husain, Hyder S. Elliptic jets. Part 1. Characteristics of unexcited and excited jets. *Journal of Fluid Mechanics* 1989, 208, 257–320 DOI:10.1017/S0022112089002843.
59. Quinn, W. R. Experimental study of the near field and transition region of a free jet issuing from a sharp-edged elliptic orifice plate. *European Journal of Mechanics - B/Fluids* 2007, 26(4), 583–614. DOI:10.1016/j.euromechflu.2006.10.005.
60. Krothapalli, A., Baganoff, D., Karamcheti, K. On the mixing of a rectangular jet. *Journal of Fluid Mechanics* 1981, 107, 201–220 DOI:10.1017/S0022112081001730.
61. Quinn, W. R. Turbulent free jet flows issuing from sharp-edged rectangular slots: The influence of slot aspect ratio. *Experimental Thermal and Fluid Science* 1992, 5(2), 203–215. DOI:10.1016/0894-1777(92)90007-R.

## Appendix: Cross-streamwise RMS velocity and Reynolds shear stress

Not only the hot-wire measurement using the I-type probe but also we used an X-type probe to obtain the statistics of the cross-streamwise velocity in the experimental spatially developing jets. Through this additional experiment, we obtain the cross-streamwise RMS velocity $v_{RMS}$ and Reynolds shear stress $\overline{u'v'}$. The results are not used to discuss the diffusion performance of the round and lobed jets but are worth showing to describe the characteristics of the jets.

The X-type hot-wire probe used in these experiments was 0251R-T5 (KANOMAX). A tungsten wire with a diameter of $5.0$ $\mu$m was glued together with spot welds in our own work. Before the measurements in the jet flows, we carefully checked the effective velocity characteristics varying with the pitching attack angle of the probe: in a uniform flow at a constant velocity, we changed the attack angle of the probe (from $-60^\circ$ to $+60^\circ$ with intervals of $5^\circ$) and the effective velocity was recorded. The obtained characteristics were used to decompose the measured velocity data into streamwise and vertical velocity components.

Although not presented here, we confirmed that the streamwise velocity statistics, $U$, $U_{RMS}$, and $r0.5$ obtained by the X-type probe measurements, were in good agreement with those by I-type probe measurements.

Figure 16 shows the radial distributions of $v_{RMS}$ and $\overline{u'v'}$ normalized by $U_C$ and $r_{0.5}$. As indicated by the error bars, the relative uncertainty of the measurements of the Reynolds shear stress using the X-type hot-wire probe might be large.

This is caused by the experimenters installing the probe onto the traverse device; the Reynolds shear stress can be more contaminated by the errors in the yawing and rolling angle of the probe than the other statistics. Similar to Fig. 8, the development is the fastest in the cases of the round and 3L lobed jets than in 6L and 6S jets. The $v_{RMS}$ and $\overline{u'v'}$ distributions of the round and 3L lobed jets at $x/D_E = 20$ are almost in self-similar distributions. We also noticed that $\overline{u'v'}$ of the 3L jet is asymmetric even in the self-similar state, unlike the others. This is considered to be related to the unequal half-width of the 3L jet shown in Fig. 9. Meanwhile, in $x/D_E \leq 5$, the maxima of $v_{RMS}$ and $\overline{u'v'}$ in the round and 3L jets are larger than those of the 6L and 6S jet. Especially, the large $v_{RMS}$ of the 3L jet at $x/D_E = 2$ is pronounced.

The same as in Fig. 16, but produced by the numerical simulations, is shown in Fig. 17. Again, we note the fast development of the round and 3L jets and the asymmetry of the Reynolds shear stress of the 3L jet. These features are as well represented in the numerical results as in the experimental results, supporting our main conclusion that the numerical simulations are a very good model of the experiments. Large $v_{RMS}$ and $\langle u'v' \rangle$ of round and 3L jets in the earlier stages can be also observed in these plots, being in good agreement with the experimental results. However, the extremely large $v_{RMS}$ of the 3L jet is absent in the current numerical result; the $v_{RMS}$ of the 3L jet monotonically increases with time as well as the others.

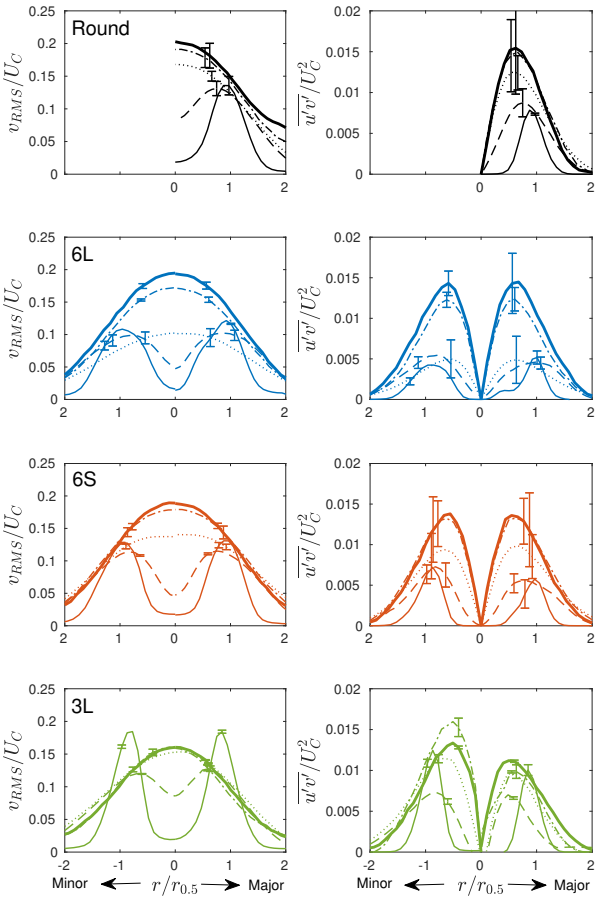


**Figure 16.** Radial distributions of $v_{RMS}$ and $\overline{u'v'}$ normalized by $U_C$ and $r_{0.5}$ at $x/D_E = 2$(thin-solid), 5(dashed), 10(dot), 20(dot-dashed), and 30(thick-solid).

## Appendix: Axis switching of temporally developing jets

Axis-switching phenomena, i.e., reversal of the large/small relationship of half-width $r_{0.5}$ on the major and minor axes, have been widely observed in non-circular jets. This is caused by the non-uniform curvature of the non-circular jets' perimeter[11].

Aleyasin et al.[13] reported that the daisy (lobed-like) jet also showed the axis-switching phenomenon in addition to the elliptic, rectangular, and triangle jets. However, Fig. 5 in Aleyasin et al.[13] shows that the non-axisymmetry of the daisy jet is much smaller than the elliptic, rectangular, and triangle jets. Consistently with this finding, Figs. 13 (a) and 14 show that $r_{0.5}$ at minor axis increases with time whereas that at major axes decreases for 6L and 6S jets, resulting in the axisymmetric mean velocity distributions. Unlike these lobed jets, 3L does not exhibit axis-switching, and $r_{0.5}$ at the major axis is always larger than that at the minor axis. However, this behavior is the same as those in Fig. 9, showing that the axis-switching is absent in 3L jet.

Therefore, it is considered that the temporally developing simulations can adequately reproduce the axis-switching phenomena of the jets. To demonstrate this, the vortex rings in the lobed jet 6L in the initial state are investigated. Figure 18 shows the isosurface of $Q$, defined in Eq. 13, illustrating the vortex rings in the lobed jet 6L at $t = 2.0$. For a clearer visualization of only the transverse vortex rings, the relatively small-scale perturbations were filtered out using the following low-pass filter technique,

$$\begin{aligned} \tilde{u}_i^L &= \mathcal{F}^{-1}(G\mathcal{F}(\tilde{u}_i)), \\ G &= \begin{cases} 1 \ (k_i < \max(k_i)/4), \\ 0 \ (\text{otherwise}) \end{cases} . \end{aligned} \tag{17}$$

Note that this filtering is independent of that for the LES. The side view on the right side of the figure shows that the lobes of the major axes of the vortex rings are tilted in the downstream direction. This is because the induced velocity is larger in the area where the curvature of the vortex is larger than that in the surrounding area, as claimed by previous studies that found the axis-switching phenomenon[58–61].

We further conducted a simulation of an elliptic jet to check the reproduction of the axis-switching of the temporally developing flows other than the lobed jets. The aspect ratio of the initial jet core is $2:1$. The vertical and horizontal lengths of the initial jet core are $D_E/2\sqrt{2}$ and $D_E/\sqrt{2}$, respectively so that the area of the exit is identical to the round jet $\pi D_E^2/4$. The other numerical conditions, such as $Re_J$, are the same as the simulations of round and lobed jets.

Figure 19 shows the vortex rings in the elliptic jet at $t = 2.0$. It is confirmed that this configuration also reproduces the large convection velocity with large vortex curvatures. However, as seen in Fig. 20, the axis-switching hardly occurs in the current elliptic jet; the inversion of half-widths in the major and minor axes is not easily achieved, and the

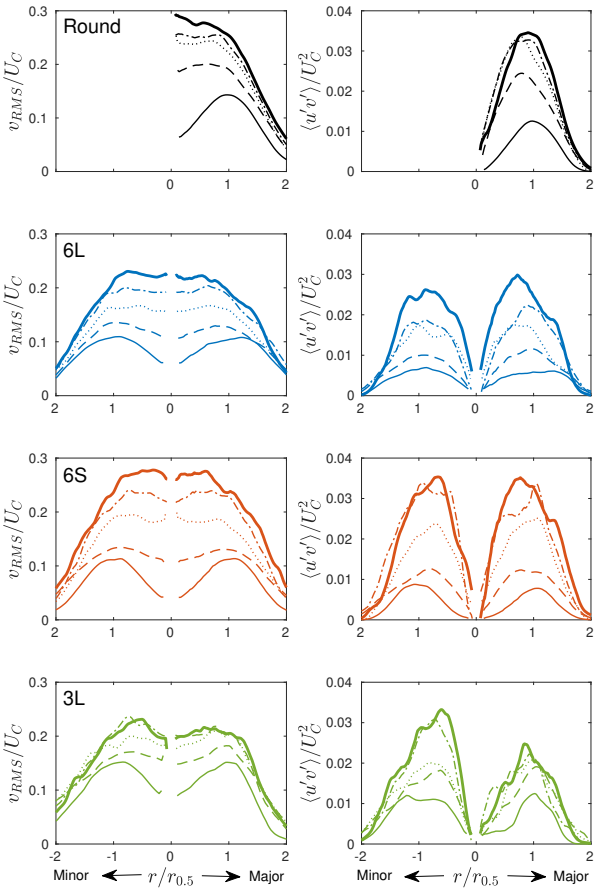


**Figure 17.** Radial distributions of $v_{RMS}$ and $\langle u'v'\rangle$ normalized by $U_C$ and $r_{0.5}$ at $t = 5$(thin-solid), $10$(dashed), $15$(dot), $20$(dot-dashed), and $25$(thick-solid).

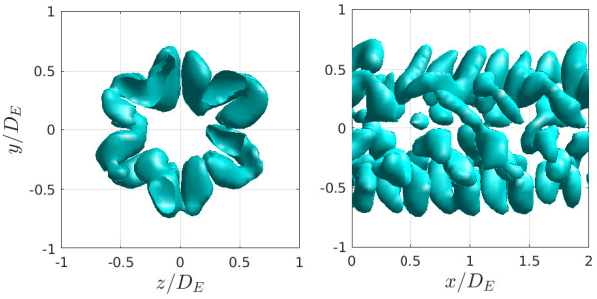


**Figure 18.** Vortex rings in lobed jet 6L at $t = 2.0$. The isosurface is set at $Q = 0.15\mathrm{max}(Q)$.

curves finally intersect at $t \simeq 25$. Although not appear in this manuscript, we confirmed such unclear axis-switching also in a temporally developing rectangular jet with the exit aspect ratio $2:1$.

In summary, we demonstrated that the temporally developing simulations can reproduce the important vortex dynamics that cause the axis-switching of the non-circular jets. However, the definite axis-switching is not always observed as a result of vortex deformation. The streamwise homogeneity of temporally developing jets might suppress the advection of swirling flows with a large axial curvature. In addition, linear spreading with streamwise distance, which appears only in spatially developing jets, might be necessary for pronounced axis-switching.

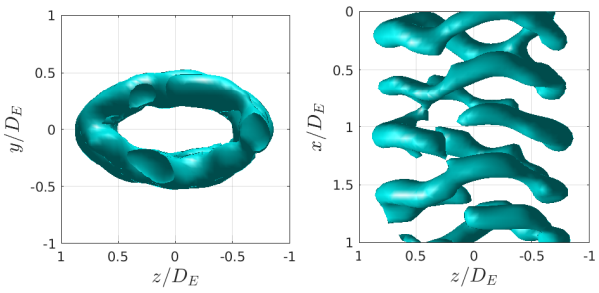


**Figure 19.** Vortex rings in a temporally developing elliptic jet at $t = 2.0$. The isosurface is set at $Q = 0.15\mathrm{max}(Q)$. The black arrow indicates the direction of the planar view.

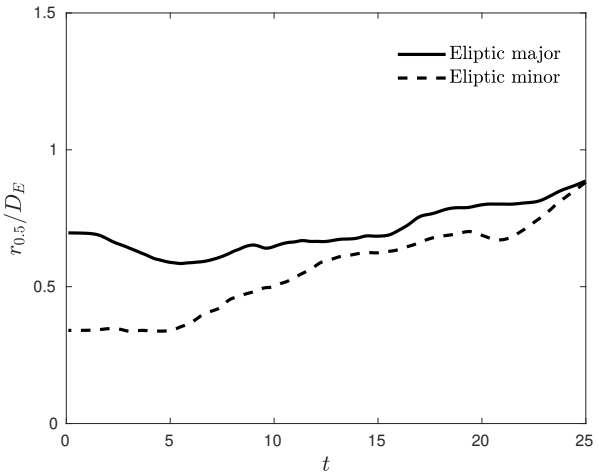


**Figure 20.** Temporal evolution of $r_{0.5}$s in a temporally developing elliptic jet

## Nomenclature

| | |
|---|---|
| $\cdots_{RMS}$ | Root-mean square. |
| $\Delta t$ | Time step. |
| $\Delta$ | Filter width for LESs. |
| $\imath$ | The imaginary unit. |
| $\langle\cdots\rangle$ | Spatial average. |
| $\mathcal{F}$ | Fourier transform. |
| $\nu$ | Kinematic viscosity of air. |
| $\overline{\cdots}$ | Time average. |
| $\sigma$ | Unbiased standard deviation of experimental results. |
| $\tau_{ij}$ | Sub-grid-scale (SGS) stress. |
| $\theta$ | Azimuthal direction. |
| $\tilde{\cdots}$ | Instantaneous quantity. |
| $a$ | Number of lobes of exit geometry. |
| $b$ | Curvature of lobes of exit geometry. |
| $C$ | Model coefficient for sub-grid-scale (SGS) stress model. |

$D_E$ Equivalent diameter of jet exit.

$f_S$ Sampling frequency.

$k_i$ Wavenumber in the $i$th direction.

$m$ Number of experimental trials.

$N_S$ Sampling number.

$p$ Static pressure per unit mass.

$r$ Radial direction.

$r_{0.5}$ Radial direction.

$Re_J$ Jet Reynolds number.

$S_{ij}$ Rate-of-strain tensor.

$T$ Sampling time.

$t$ Time

$U$ Mean streamwise velocity.

$u$ ($u_1$) Streamwise velocity component.

$U_C$ Centerline mean streamwise velocity.

$U_J$ Initial jet velocity.

$v$ ($u_2$) Vertical velocity component.

$V_r$ Mean radial velocity.

$v_r$ Radial velocity.

$w$ ($u_3$) Spanwise velocity component.

$W_{ij}$ Rate-of-rotation tensor.

$x$ ($x_1$) Streamwise direction.

$x_T$ Traveling distance.

$y$ ($x_2$) Vertical direction.

$z$ ($x_3$) Spanwise direction.